Hindawi Publishing Corporation
Advances in Acoustics and Vibration
Volume 2011, Article ID 984596, 15 pages
doi:10.1155/2011/984596

Research Article

Performance of an Ultrasonic Imaging System Based on a 45-MHz Linear PVDF Transducer Array: A Numerical Study

Eivind Brodal,[1] Frank Melandsø,[2] and Svein Jacobsen[2]

[1] *Department of Engineering and Safety, University of Tromsø, 9037 Tromsø, Norway*
[2] *Department of Physics and Technology, University of Tromsø, 9037 Tromsø, Norway*

Correspondence should be addressed to Eivind Brodal, eivind.brodal@uit.no

Received 14 December 2010; Accepted 30 March 2011

Academic Editor: Luc Gaudiller

New designs of high-resolution ultrasonic imaging systems that operate in the 30–100 MHz region, for example, those based on linear transducer systems, are currently being investigated for medical purposes. Acoustic waves with frequencies in this range can detect microscopic structures in human tissue but will typically only penetrate a few mm because of large attenuation. However, this is sufficient for a diagnostic ultrasound scan of human skin. The signal-to-noise ratio and the focusing properties of the scanner are critical factors in dermatology, which are determined by the transducer design. A linear pulsed PVDF transducer array with a center frequency around 45 MHz is studied by applying numerical simulations, based on the finite element method (FEM), of this electromechanical system. Tx-beamforming properties of linear arrays with one, three, five, and seven active elements are investigated at different depths. The image quality obtained from synthetic Rx-beamforming, using responses from five electrodes, is estimated from reconstructed images of 25–100 μm thick objects. The axial and lateral resolutions of these images are found to be similar with the Tx-beamforming resolution parameters estimated from the time-derivative of the pressure beams.

1. Introduction

Medical diagnostic based on high-resolution images obtained from ultrasound scanning in the lower VHF range (30 MHz to 100 MHz) is a relatively new technique still under development [1–5]. A major problem one encounters in systems operating at such high frequencies is the attenuation in human tissue, which severely reduces the signal-to-noise ratio and the penetration depth of acoustic waves. That is, the range of the high-frequency waves are mostly affected, since acoustic damping in human tissue increases with frequency. On the other hand, high frequencies must be generated in order to detect microscopic structures which can be vital in a medical diagnosis. As a consequence, only a few mm into human tissue can be scanned in order to maintain a sufficient image quality. Examination of skin diseases, for example, tumors, is one example, where such high-resolution systems can be applied [6]. The size and geometry of suspicious structures are important factors when classifying and monitoring skin diseases. Therefore, an imaging system with high-resolution in both axial and lateral directions is needed when investigating such microscopic tissue parts. Hence, the transducer elements must generate short acoustic pulses, while the overall scanning system should have satisfactory focus and signal-to-noise properties. Dermatological applications and skin structures, as well as image resolution and depth of penetration related to existing ultrasound systems operating at frequencies between 7.5 MHz and 100 MHz, are discussed in [7]. Different techniques used in skin imaging are explained in [8].

The image quality of the ultrasound scan is strongly related to the design of the transducer system, and research today is devoted to building efficient ultrasound scanners which can be used in detecting, measuring, and localizing skin tumors. The performance of single transducer elements with a fixed focus suffers from the tradeoff between a high resolution and the depth of penetration. An annular transducer array has dynamical focus properties in the depth direction which solves this problem but still has to be mechanically moved [9]. The 2D beam steering properties of linear transducer arrays have shown growing interest within this field in recent years [10], since such arrays can scan a

skin region faster while avoiding problems associated with mechanical scanning. New and improved linear transducer array designs are currently under development; for example, an array with 256 elements and a 40 μm electrode pitch was presented in [11]. PVDF-based transducer arrays are frequently selected, since they have excellent broadband qualities and are relatively inexpensive compared to other piezoelectric transducer systems [12, 13].

The image quality obtained from transducer arrays depends strongly on the number of active transmitting (Tx) and receiving (Rx) elements. Ultrasonic waves produced by an array can be focused at different spatial points by time delaying the transitions from the individual elements [14]. The shape and strength of the focused beam depend both on the distance from the transducer array and the number of active transducer elements. The full pulse width at half maximum (FWHM) in the lateral and axial directions of the focused signal generated from Tx-beamforming is often used to describe the resolution of the imaging system. The ultrasound scan performance of linear transducer arrays with a 9 μm thick PVDF film and a 150 μm electrode pitch is discussed in this paper by evaluating such resolution parameters. Acoustic pulses with center frequencies around 45 MHz are transmitted into human skin when the electronic push-pull drivers, connected to the transducer elements, are activated. A different set of resolution parameters, derived directly from reconstructed images of small objects/structures using synthetic Rx-beamforming, is also discussed and compared with the resolution parameters obtained from Tx-beamforming.

The partial differential equations (PDEs) describing the electromechanical transducer systems are assumed to be linear. A 2D model based on the plane strain approximation can be used to describe these transducer arrays, since the length of the transducer elements (2 cm) are large compared to the size of the transducer parts in the other two directions. The objects being scanned in this paper have been given geometries, where the plane strain approximation is valid. The materials involved are assumed to be homogeneous, even at the microscopic level, unless otherwise stated. Numerical simulations of these (2D) piezoelectric systems are conducted in the time domain with Comsol Multiphysics (http://www.comsol.com); a commercial software solving partial differential equations based on the finite element method (FEM) [15]. Note that a synthetic beamforming approach is chosen over simulations of real-time beamformers. Real-time beamformers typically transmit a very large number of focused beams over a short time period; for example, 100,000 focused waves are created each second when there is a 10 μs time interval between transmissions. Accurate numerical FEM simulations of a single beam, on the other hand, can be in the order of hours, making the electronic phase-delayed scanning approach extremely time consuming to model. However, different simulations where only one transducer element is activated at a time can be combined synthetically to reproduce a real-time beamformer system, since the PDEs are linear.

Analytical solutions of multilayered (1D) longitudinal strain problems can, for example, be obtained from the matrix model based on the impedance matrix [16]. The FEM simulations have been verified and found to produce excellent solutions by solving an identical multilayered longitudinal strain problem with both the FEM on a 2D geometry and the 1D matrix model. We have partially documented this for a similar problem in [17].

The transducer system is described in Section 2. Parameters describing the spatial size and strength of the focused beam at various depths in human skin are computed in Section 3, using Tx-beamforming which has up to seven active transducer elements. Responses from 25–100 μm thick objects and the quality of the reconstructed images (based on synthetic Rx-beamforming including responses from five elements) are estimated and discussed in Section 4.

2. Model of a High-Resolution Ultrasound Diagnostic System

The transducer design illustrated in Figure 1 can be used in high-resolution ultrasound diagnostic of human skin. This is a linear transducer array with a 9 μm thick PVDF film and a 150 μm electrode pitch. The electrode pattern located on the backside of the PVDF film consists of 2 cm long, 100 μm wide and 2 μm thick copper elements. A 0.1 μm thick gold film is connected to the front side of the PVDF, and a thick epoxy layer serves as a backing. The thin gold layer has only minor effects on the transducers frequency response at frequencies below 60 MHz [18] and is, therefore, neglected in the numerical simulations. These simulations are based on the FEM which solves the linear electromechanical PDEs introduced in the piezoelectric plane strain model [19], where also acoustic attenuation is included. Nonlinear effects have been neglected. The material constants involved in the numerical computations are given in Table 1, and are assumed to be homogeneous. That is, microscopic structures, like hair follicles, are neglected in the skin model.

Acoustic attenuation in human skin is typically in the range of 1–3 dB/(cm MHz) [23]. Elderly people often have skin with a smaller damping, but there are large variations in every age group as well. The two-way attenuation in human skin is illustrated in Figure 2 and shows that the penetration depth is reduced significantly at higher frequencies. Attenuation in PVDF, epoxy and copper are based on data from [27–29]. Note that these attenuation coefficients are estimated from experiments below 15 MHz.

The transducer array transmits acoustic pulses when the electronic push-pull drivers are activated (t_0). The electric potential at the active copper electrode is approximated as a step-like signal in the numerical simulations

$$U(t) = \frac{U_0}{2}\left[1 + \operatorname{erf}\left(\frac{(t - t_0)}{\sigma\sqrt{2}}\right)\right], \tag{1}$$

where "erf" is the time-integrated Gaussian function with standard deviation σ, also known as the Gauss error function. The gold electrode is connected to ground. Note that the electric potential $U(t)$ is a step function when $\sigma \to 0$. The individual transducer elements are driven by sources with $\sigma = 5$ ns in the simulations.

Table 1: Material constants used in the numerical simulations [20–23]. A PVDF film with Young's modulus and electromechanical coupling factor of 4.0 GPa and 14%, respectively, was chosen. Properties of PVDF films vary depending on the processing technique, temperature, frequency, and age [24–26]. Attenuation in PVDF, epoxy, copper, and human skin are based on data from [23, 27–29].

			PVDF	Epoxy	Cu	Au	Skin
Density	ρ	$(10^3\ \mathrm{kg/m^3})$	1.78	1.20	8.96	19.3	1.00
Young's modulus	E	$(10^9\ \mathrm{Pa})$	4.0	3.0	120	79	—
Poisson's ratio	γ	$(-)$	0.20	0.34	0.31	0.46	—
Longitudinal wave speed	V_l	$(10^3\ \mathrm{m/s})$	1.6	2.0	4.3	4.4	1.54
Transverse wave speed	V_t	$(10^3\ \mathrm{m/s})$	1.0	1.0	2.3	1.2	0
Attenuation	α	$(\mathrm{dB/(cm\ MHz)})$	10	1.2	0.03	—	2
Piezoelectric const.	e_{31}	$(\mathrm{C/m^2})$	0.004	—	—	—	—
Piezoelectric const.	e_{33}	$(\mathrm{C/m^2})$	−0.096	—	—	—	—
Piezoelectric const.	e_{15}	$(\mathrm{C/m^2})$	0	—	—	—	—
Permittivity	$\epsilon^S_{11}, \epsilon^S_{33}$	$(10^{-12}\ \mathrm{F/m})$	106	—	—	—	—

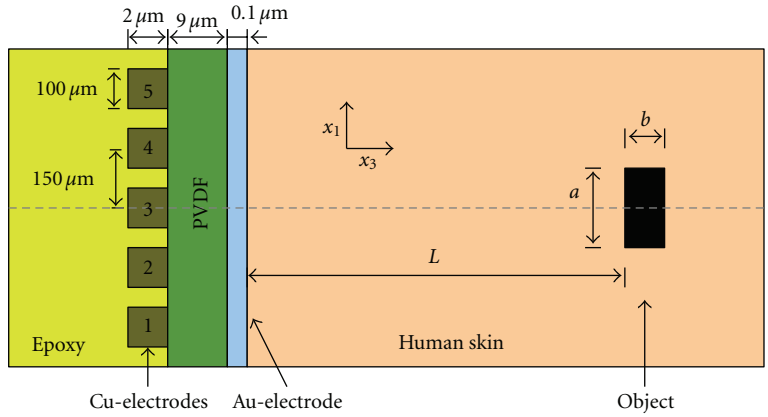

Figure 1: Cross section of a linear transducer array with five elements (copper electrodes). An object with a rectangular cross section ($a \times b$) is located in the human skin sample at depth L.

Figure 3 illustrates the layers in a design of a single transducer element with wide copper electrodes which can be described by a 1D longitudinal strain model. The frequency response of longitudinal strain transducer systems can be found analytically [19]. The copper electrode current $I(t) = AJ(t)$ (with surface area A) is then computed through an inverse discrete Fourier transformation. Figure 4 illustrates the applied electric potential together with the generated copper electrode current. The backscattered echo from a metal object (assumed to give a total reflection) located at 0.3 mm below the surface of the skin is illustrated in Figure 5. Note that the center frequency of the response, produced from the $\sigma = 5$ ns source, is around 45 MHz. Figure 5 also illustrates how significantly the attenuation in human skin and in the PVDF film affect the response at such high frequencies. The frequency content of the response above 60 MHz is already small at a depth of 0.3 mm. Frequencies less than 10 MHz do not contribute much either, since the PVDF layer is thin (only 9 μm).

The linear attenuation coefficients are replaced for computational reasons by second-order approximations in the FEM model of the plane strain transducer array systems illustrated in Figure 1. These second-order attenuation coefficients are ordinary Rayleigh damping parameters and can be included directly in FEM schemes operating with only real numbers [30]. Rayleigh damping parameters which are exact at 15 MHz and 45 MHz are chosen, since they are relatively accurate approximations for frequencies between 10 MHz and 60 MHz (see Figure 6). Open boundary conditions are applied in the FEM scheme. Symmetric beamforming problems are investigated. Symmetry condition in the lateral direction, going through the center of the object illustrated in Figure 1, significantly reduces the memory usage and the number of computations needed.

3. Tx-Beamforming

Image quality is primarily determined by the individual transducer elements and the overall focusing properties of the transducer array. The pressure and its time derivative, generated from a single transducer element, are shown at different locations in Figure 7. Constructive interference of the acoustic waves generated from the individual transducer elements are obtained at different positions by activating them in a certain order (Tx-beamforming). For example, the illumination profiles shown in Figure 8 are obtained by delaying the transmissions from five active transducer

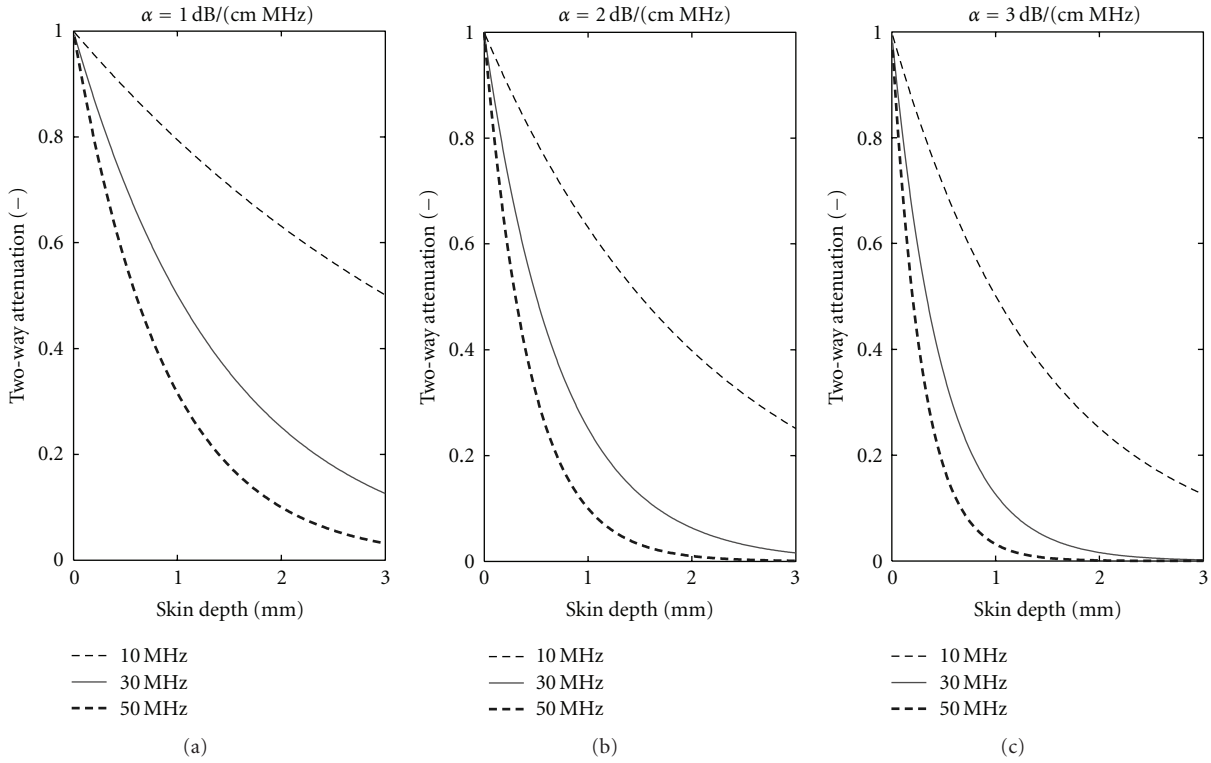

Figure 2: Two-way attenuation in human skin.

Figure 3: Longitudinal strain transducer system.

elements with the time it takes a wave to propagate from the centers of the different transducer elements to the focal point. This approach is chosen for its simplicity and is accurate for point sources. However, the elements are 100 μm wide and approximately 10 μm thick (see Figure 1). The problem related to the method we have used is clearly seen in Figure 8 when illuminating the coordinate (0.2, 0.0) mm, which is relatively close to the transducer array. Here, acoustic waves are shifted relatively to the focal point because of the lateral width of the individual transducer elements, that is, especially the waves generated from the transducer elements located further away from the center of the beam. Note that this problem is less important in conventional linear arrays since they operate at a much lower resolution. While in high-resolution scanners the fabrication technology is often a limiting factor. A better, but more complex, focusing algorithm can be based on a more accurate propagation pattern of the acoustic waves generated from such transducer elements. Different illumination profiles of the linear transducer array illustrated in Figure 1 can be seen in Figures 8 and 9. Note that these figures only show a smaller area around the focused signals; that is, only a section of the geometry is simulated in Comsol.

The magnitude of the pressure in the focused ultrasonic beam is plotted in Figure 8. Contour lines showing the FWHM, and the smallest rectangle enclosing these contours, are included in these plots. The rectangle has length λ_1 in the lateral direction (x_1) and length λ_3 in the axial direction (x_3) of the linear transducer array. The lateral and axial resolution parameters λ_1 and λ_3 at different depths are plotted together with the signal strength in Figure 10 for linear transducer arrays with seven or less active transducer elements. At depths between 0.5 mm and 1.0 mm, the resolution obtained from systems with five active transducer elements is better than 50 μm in the axial direction and better than 150 μm in the lateral direction (see Figure 10). However, images with significantly better resolution are typically produced from electrode currents responses. We believe that this difference is mainly due to the filter effect caused by the transducer when converting the acoustic signal into electric current [31]. Note that the electrode current response in the longitudinal strain system, for example, shown in Figure 5, has a similar shape as the time derivative of the pressure at ($x_3 = 0.6$ mm and $x_1 = 0$ mm), as illustrated in Figure 7. The current responses have a higher center frequency than the pressure and have, unlike the pressure signal, a maximum magnitude at the center of the pulse (see Figure 7). Resolution parameters (λ_1^* and λ_3^*) based on $\partial p/\partial t$ instead of p are shown in Figure 11 and are better than 32 μm and 110 μm in the axial and lateral directions at depths up to 1.0 mm when three or more elements are activated. Note that the FWHM definition of

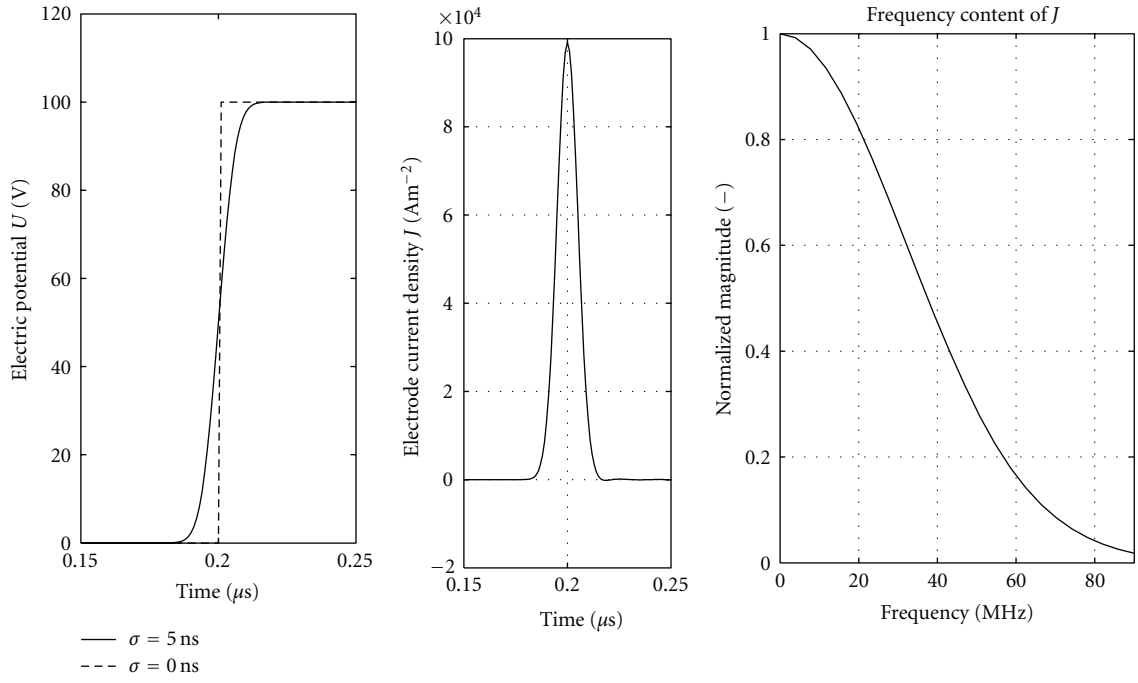

FIGURE 4: Electric potential U at $t_0 = 0.2\,\mu$s (a). The electrode current density response (in the longitudinal transducer system) and its frequency spectrum are shown in (b) and (c), respectively.

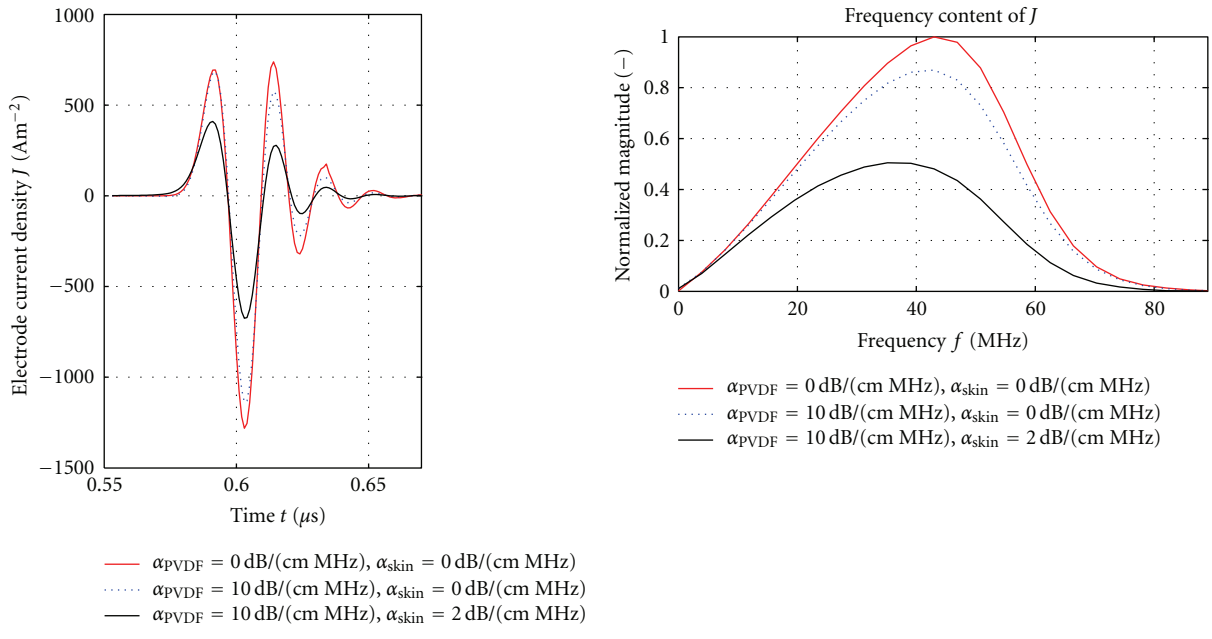

FIGURE 5: Electrode current density produced from a total reflection at depth 0.3 mm in human skin (longitudinal strain system). The effects from attenuation in human skin (α_{skin}) and in PVDF (α_{PVDF}) are illustrated.

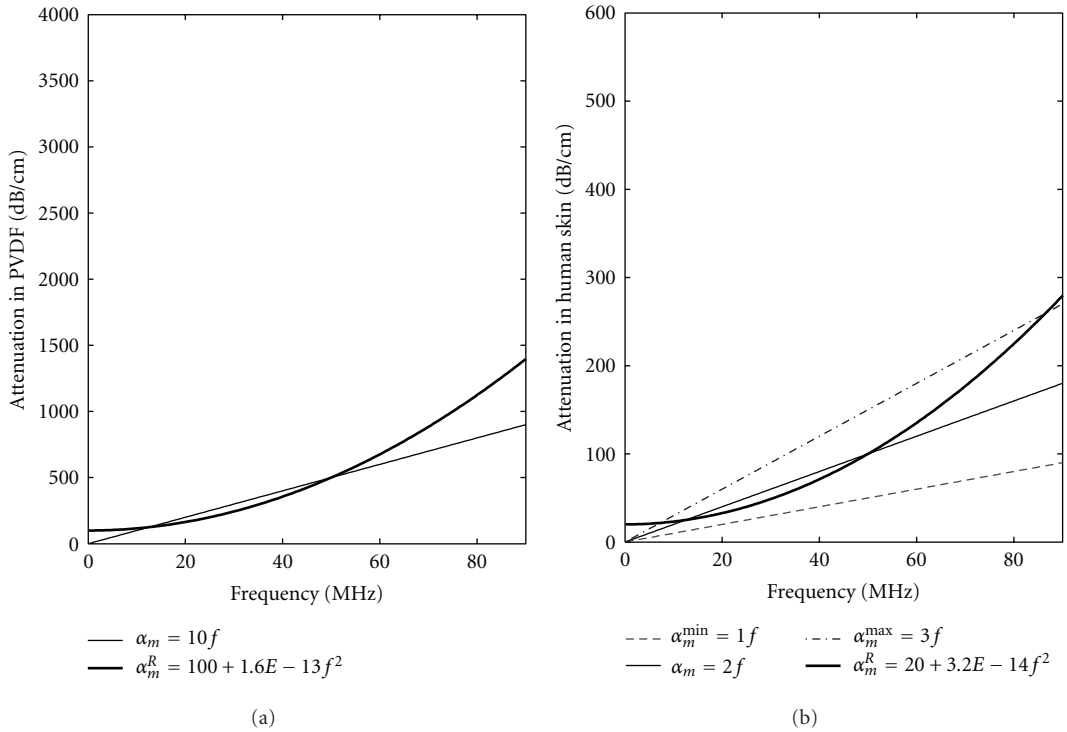

FIGURE 6: Rayleigh damping approximations α_m^R of the linear attenuation $\alpha_m = \alpha f$ in PVDF (a) and human skin (b). Variations of the linear attenuation in human skin (1–3 dB/(cm MHz)) are also illustrated.

these resolution parameters are sensitive to small variations, since local extremal points can either be less or greater than the half maximum of the pulse. Even though the element spacing is much greater than half a wavelength, the grating lobes are relatively small due to the system's excellent quality factor (see Figure 5).

Figure 11 shows that the strength of the focused signals is increased by activating a larger number of transducer elements (n_e). At large depths the strength is almost proportional to n_e. The axial resolution obtained from this transducer array is often significantly better than the lateral resolution. The axial resolution which can be obtained at a certain location is typically similar to (limited by) the FWHM of the pulse generated from the nearest transducer element, for example, illustrated in Figure 7 ($0.02\,\mu\text{s}\cdot 1540\,\text{m/s} \approx 31\,\mu\text{m}$). Note that it is also similar to the wavelength of the center frequency of the current response ($1540\ \text{ms}^{-1}/45\,\text{MHz} \approx 34\,\mu\text{m}$). Note that the axial resolution parameter in Figure 11 does not converge when focusing at small depths. In this region the FWHM sometimes only includes the main peak of the generated pulse in the axial direction, that is, less than half a wavelength. However, the FWHM typically also includes the second strongest peak (see Figure 7), and therefore has an axial resolution close to a wavelength. The non-convergence seen in Figure 11 is due to a small noise, which arises because the transducer elements are not point sources. Near the transducer array, the lateral resolution is limited by the 0.1 mm wide copper electrodes (i.e., the lateral dimension of the individual transducer elements). Deeper into the skin, the lateral beam width increases and shows a (focal depth)/(lateral transducer array dimension) dependence. Figures 10 and 11 illustrate how the lateral resolution at greater depths is improved by activating a larger number of elements. Transducer elements located far from the focus will contribute less, and are out of reach when scanning at shallow skin depths. For example, only one electrode contributes at depths less than 0.1 mm. However, the FWHM Tx-beamforming resolution parameters show that the resolution obtained from a single element is very low at larger depths, and can therefore only be used in the near-field of the transducer element.

4. High-Resolution Ultrasound Scanning of Skin Using Rx-Beamforming

The linear transducer discussed in the previous section can be used in high-resolution diagnostic ultrasound scans of human skin. Figures 10 and 11 show that a linear transducer array with five active elements is a good choice for scanning up to depths of 1 mm, and we will now study its capability of detecting small objects in human skin with density $\rho^{\text{object}} = 1000\,\text{kg/m}^3$ and longitudinal wave speed $V_l^{\text{object}} = 1600\,\text{m/s}$. That is, the acoustic impedance of these objects is only 3.9% larger than human skin. The difference in acoustic impedance between skin tumors and normal skin is often of this order or even smaller [13] (Figure 4). The backscattered signals are thus weak, and an accurate FEM scheme is, therefore, needed to model the response.

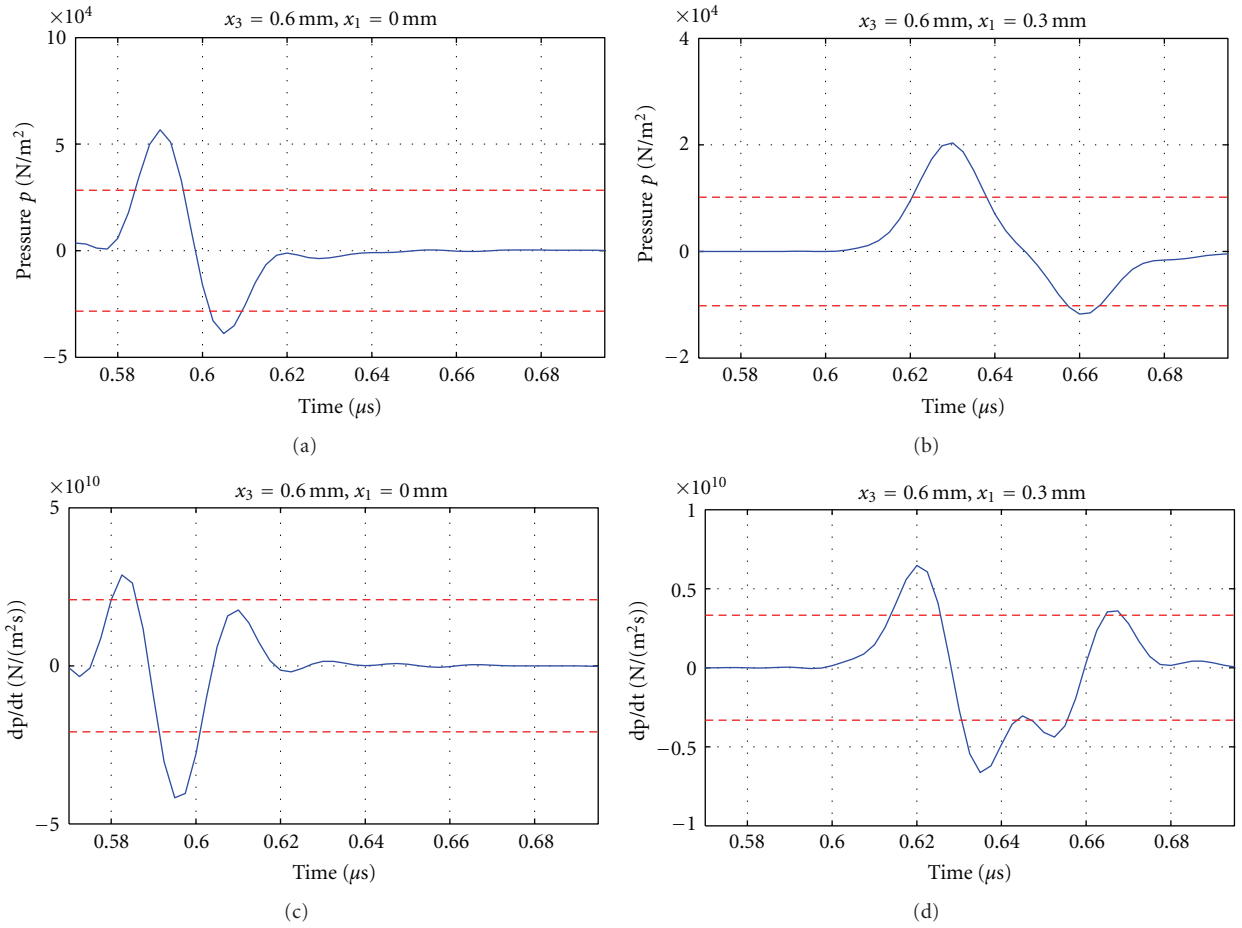

FIGURE 7: Acoustic pressure generated from a single transducer element (a, b) and its time derivative (c, d) at different coordinates (x_3,x_1) relative to the center of the transmitting transducer element. Red lines are (±) half maximum values of the pulse.

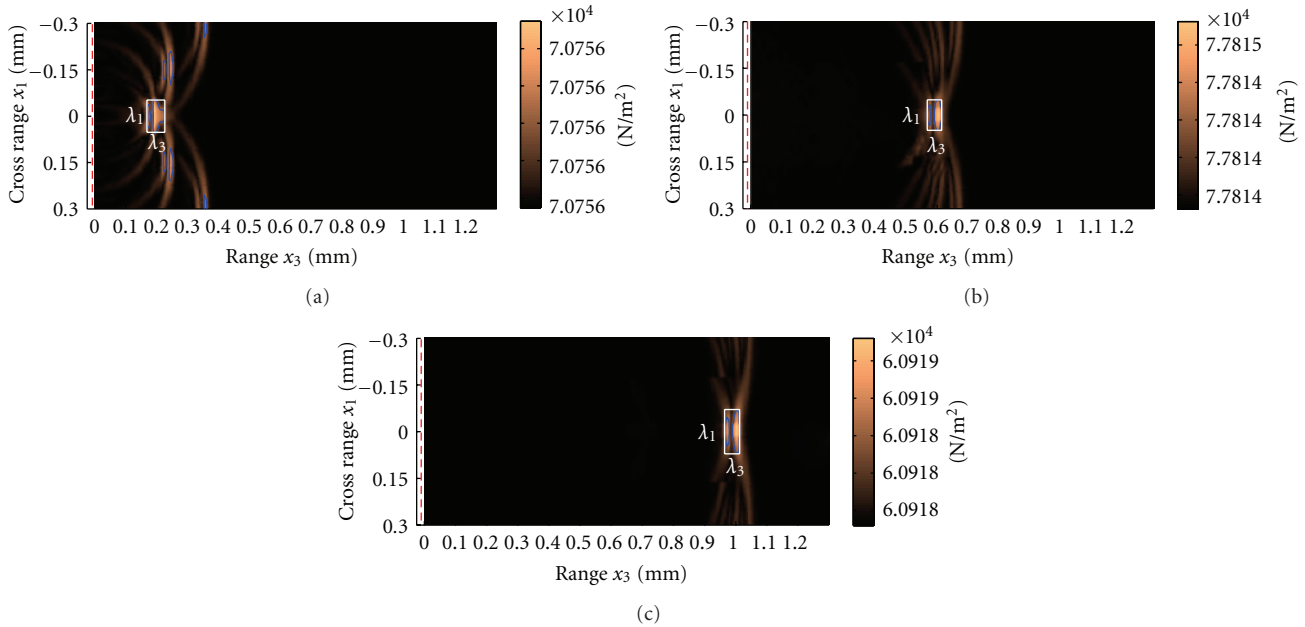

FIGURE 8: Magnitude of the acoustic pressure ($|p|$) generated from phase-delayed transducer elements illuminating the coordinates (0.2, 0.0) mm, (0.6, 0.0) mm, and (1.0, 0.0) mm. The smallest rectangles (white) enclosing the FWHM contour plots (blue) are included.

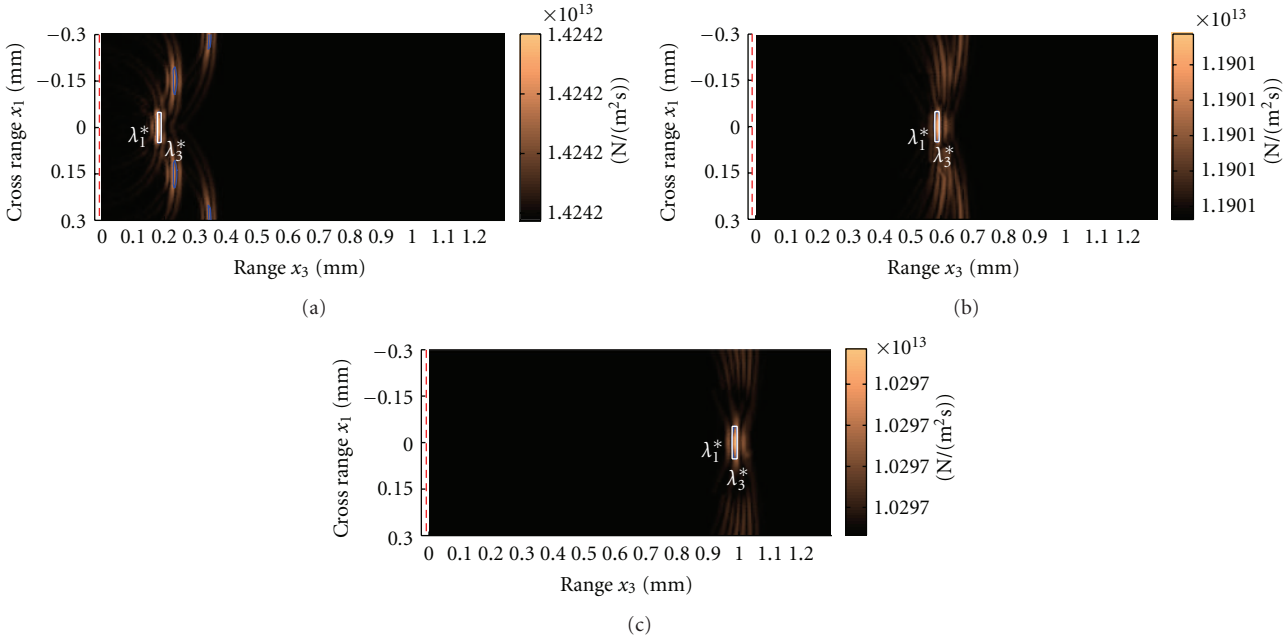

FIGURE 9: Magnitude of the acoustic pressure ($|\partial p/\partial t|$) generated from phase-delayed transducer elements illuminating the coordinates (0.2, 0.0) mm, (0.6, 0.0) mm, and (1.0, 0.0) mm. The smallest rectangles (white) enclosing the FWHM contour plots (blue) are included.

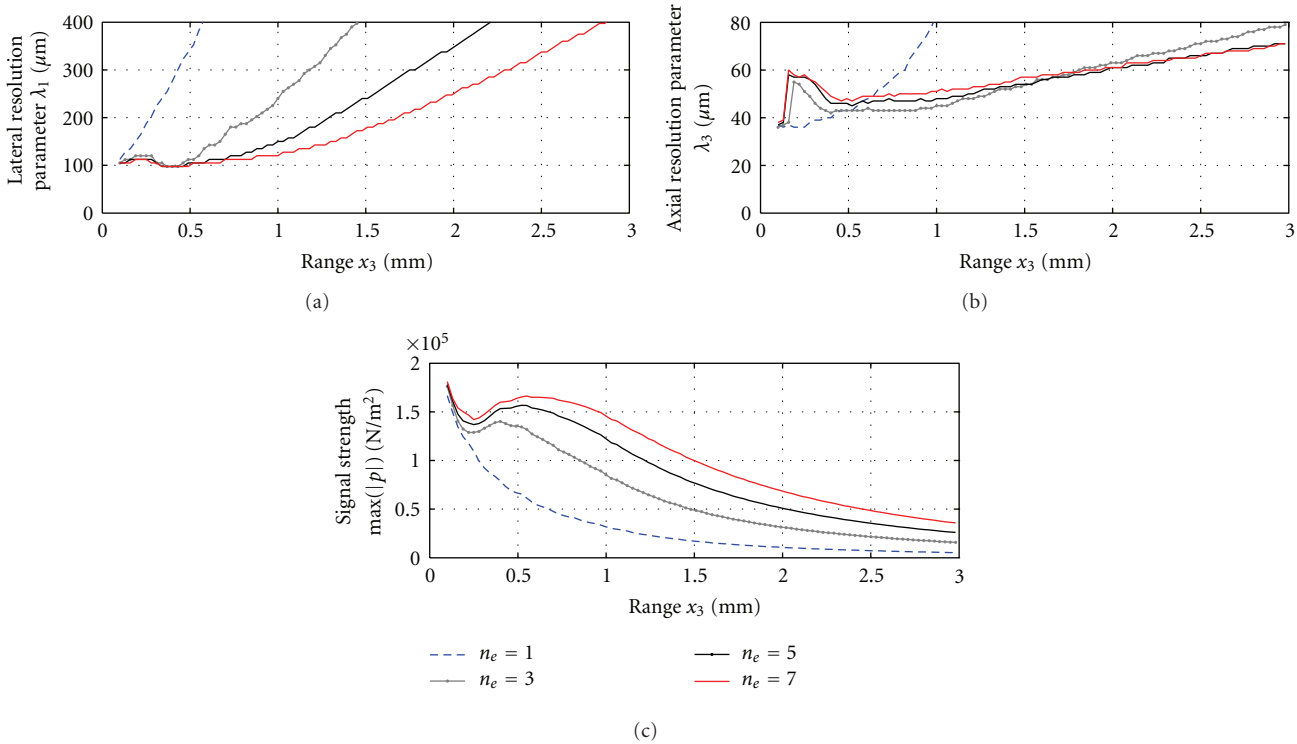

FIGURE 10: Illumination parameters based on the pressure (p) beam profile created from n_e phase-delayed transducer elements focusing at the location $(x_3, 0)$.

A typical acoustic pressure, generated in human skin by a single transducer element, is shown in Figure 12 at four different times (only the lower half of the system is plotted due to symmetries). A long skin object with a $2.5E-9\,\text{m}^2$ rectangular cross section (having lateral length $a = 25\,\mu$m and axial thickness $b = 100\,\mu$m) is located at 0.6 mm depth (L); see Figure 1. The weak backscattered waves reflected by this structure can also be seen in Figure 12, and the currents produced at the five copper electrodes are illustrated in Figure 13. The electrode numbering is shown in Figure 1.

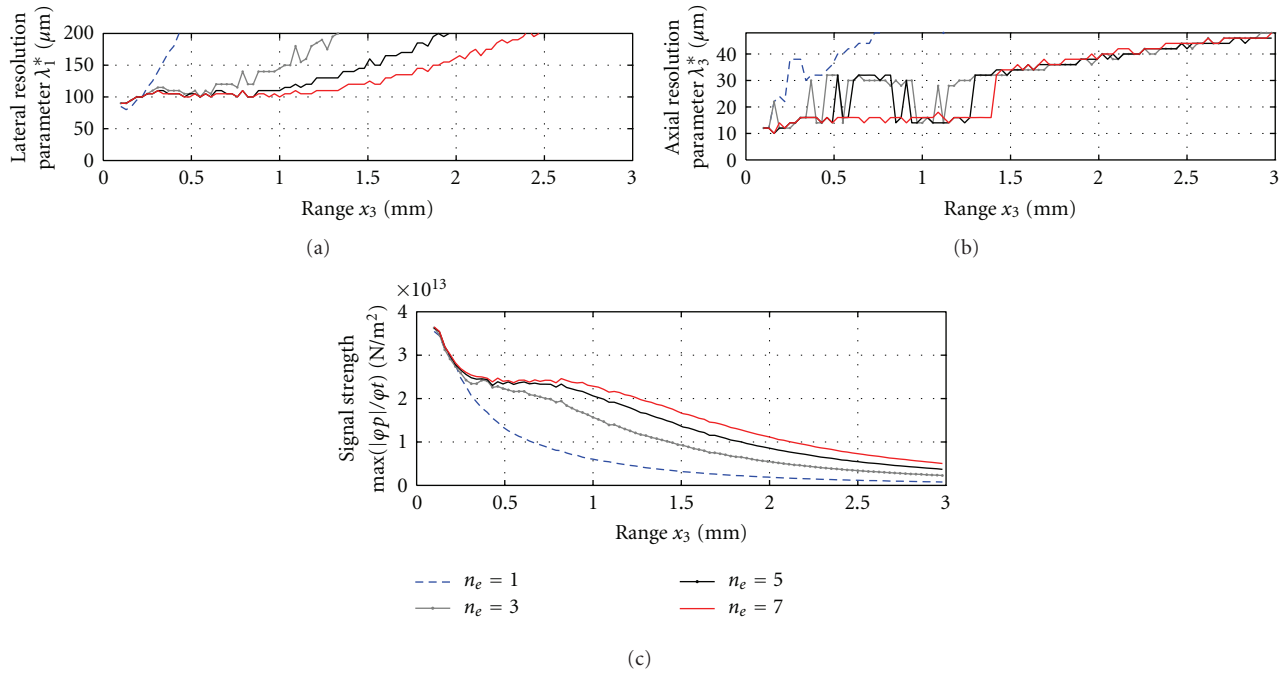

FIGURE 11: Illumination parameters based on the time derivative of the pressure ($\partial p/\partial t$) beam profile created from n_e phase-delayed transducer elements focusing at the location $(x_3, 0)$.

Figure 12 shows that the strength of the backscattered pressure wave is only about 0.2% of the initial pressure wave generated from the transducer. The backscattered waves loose their strength quickly if the object is found deeper in the skin. For example, the strength of the pressure is reduced to less than a tenth if this object is relocated at 1.0 mm depth. That is, in this case, the received pressure wave is less than ~0.02% of the transmitted wave. This is mainly caused by the large acoustic damping properties of human skin, but wave diffraction is also a contributing factor. Note that Figure 2 shows that about 70% of the signal strength is lost, due to attenuation, when a plane wave around 45 MHz propagates a distance of (2×0.4) mm.

Electric currents produced at the copper electrodes by acoustic echoes reflected from long objects with $2.5E-9$ m^2 rectangular cross sections $(b \times a)$ that are located at $L = 0.6$ mm and $L = 1.0$ mm depths, are plotted in Figures 13 and 14. Only one transducer element, located directly in front of the object, is transmitting. The responses $(I_1 - I_5)$ at the five copper electrodes are influenced by attenuation in the skin, diffraction of the acoustic waves and the individual transducer elements orientation/location, but also depend strongly on the object's geometry, size and location.

Responses from objects are weakened drastically with increased depth (L). For example, Figures 13 and 14 show that the electric currents generated by backscattered echoes from objects located at 1.0 mm depths are less than 10% of the responses produced from identical objects located at 0.6 mm depths and also contain a much smaller portion of high frequencies above 45 MHz. The electric currents at the five electrodes illustrate that the main echoes produced from the front and backside of these thin structures can be recognized and separated. The FWHM of the front and backside echo responses in I_3 are both approximately 0.02 μs. Note that 0.02 μs·1540 m/s $\approx$ 31 μm, which is approximately the wavelength of a 45 MHz wave in human skin (34 μm). It is even possible to separate the two pulses from the thinnest objects with thickness $b = 25\,\mu$m, which are even smaller than the size of the axial resolution parameter λ_3^* found at 0.6–1.0 mm depths. However, these echoes will overlap more if the thickness is further reduced (see Figures 13 and 14). Constructive interference between these echoes will occur in the FWHM region of the current responses (with $b \approx 15\,\mu$m), but the front and backside of the object cannot be separated. Destructive interference between reflections from the front and backside reduces the response strength of the total echo from even thinner objects, making them more invisible in the ultrasound scan. Interference patterns between the echoes from the front and backside of the object can be recognized in the frequency spectra of the responses plotted in Figures 13 and 14. For example, frequencies $f_n = 16\,n$ MHz are removed from the signal produced from $b = 50\,\mu$m thick objects, since destructive interference will occur in the backscattered signal at frequencies $f_n = nV_l^{\text{object}}/(2b)$, where n is an integer.

Figures 13 and 14 illustrate that the response depends on angle θ_i^L between the center of transducer element number i and the center of the object ($\tan\theta_3^L \approx |i-3| \cdot 0.15$ mmL). The frequency content of the responses produced at electrodes further away from the object (large θ_i^L) are shifted downwards, and the frequencies above 35 MHz which are present in I_3 ($\theta_3^L = 0$) are almost removed in I_1 and I_5.

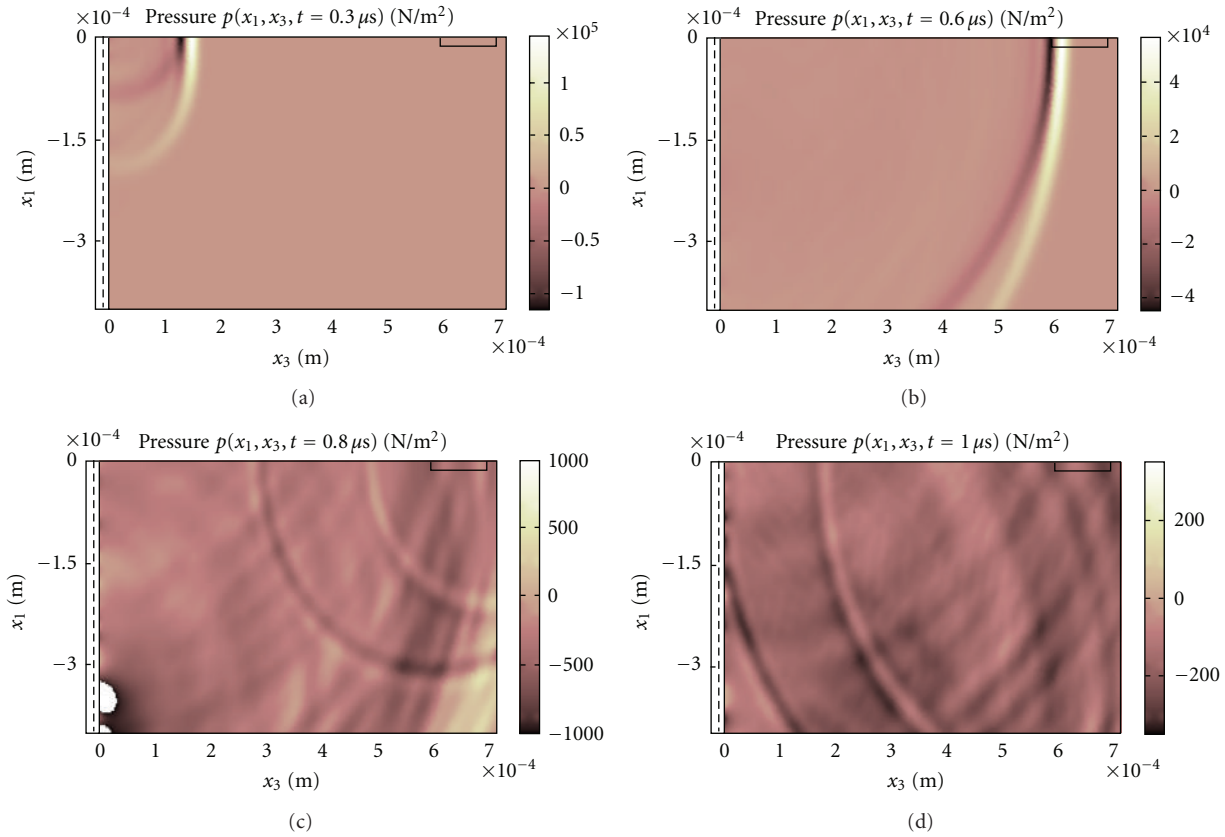

FIGURE 12: The acoustic pressure, generated from only one active transducer element, in human skin containing a object is shown at four different times. Due to symmetries in the lateral direction, going through the center electrode ($x_1 = 0$), only the lower half of the transducer system in Figure 1 is shown.

The time-duration of the current responses produced by the backscattered waves are larger at the electrodes located further away from an object, since the acoustic echoes will spend longer time inside these transducer elements, which are approximately 0.1 mm wide and 0.01 mm thick, when θ_i^L is large. This is illustrated in Figure 12. Figures 13 and 14 also show that the strength of the responses $(I_1 - I_5)$ differs more if the objects are located close to the transducer array; that is, θ_i^L is large ($\theta_1^{0.6\,\text{mm}} \approx 27^\circ$ and $\theta_1^{1.0\,\text{mm}} \approx 17^\circ$). For example, with $L = 0.6$ mm the strength (signal-to-noise ratio) of I_1 is less than a fourth of I_3, while these responses are more similar in strength if the objects are relocated at $L = 1.0$ mm. Hence, a larger number of transducer elements can be activated when scanning deeper into the skin.

Images based on backscattered signals can be reconstructed synthetically by adding time-delayed electrode responses computed by activating one transducer element at a time. Such images of human skin (including only a single object) are reconstructed in Figure 15 from a delay-and-sum (DAS) algorithm using the five copper electrode current responses plotted in Figures 13 and 14. That is, these images are based on synthetic Rx-beamforming where only one transducer element is transmitting. Each pixel is computed as (the magnitude of) an instant sum of a certain time-combination of the currents, using a time gain compensation (TGC) $\widetilde{I}_i = I_i \cdot \exp(\alpha_w t)$ with $\alpha_w = 2.5\,E6$ 1/s. The currents generated by the echoes are shifted by the time it takes a wave to propagate (at 1540 m/s) from the center of the transmitting transducer element to the location of the pixel and back to the center of the receiving transducer element. Only the back and front sides of the objects (parallel to the transducer) appear in the reconstructed images in Figure 15, since we have used a simplified homogeneous skin model. The two other sides do not reflect enough energy to be detected by scans from this direction. However, the parts of the structures which appear in these images, at depths around 0.6 mm and 1.0 mm, are all reconstructed relatively accurate by the scan. For example, the uncertainties/errors in the localization based on the FWHM plots of the back and front sides of the objects (i.e., the visible structures) are ($x_3 \pm 15\,\mu$m, $x_1 \pm 40\,\mu$m) or less in all the reconstructed images presented in Figure 15. Note that the localization errors are different in each image, since they are based on responses which strongly depend on the backscattering objects. An alternative method of describing the quality of an imaging system is to look at a new set of resolution parameters defined from the worst case of the localization errors ($x_3 \pm \widehat{\lambda}_3/2$, $x_1 \pm \widehat{\lambda}_1/2$). These resolution parameters can also be viewed as a measurement of the minimal separation distance between two structures in order for them to both appear individually in the reconstructed images and are relatively similar to the worst case Tx-beamforming resolution parameters based on

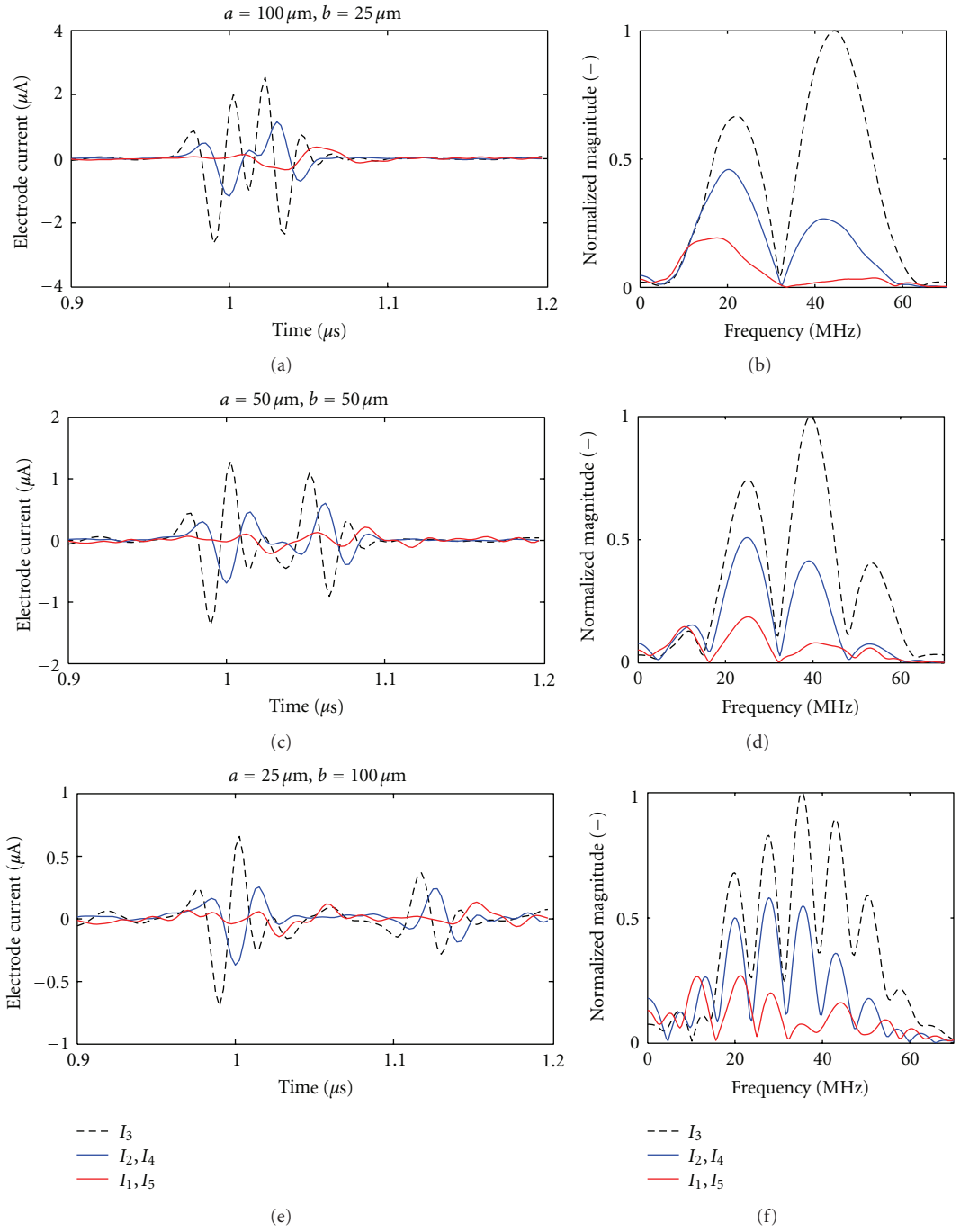

FIGURE 13: Electric currents, at the five copper electrodes, generated from the echo produced by long objects with rectangular cross section ($b \times a$) located at depth $L = 0.6$ mm (electrode numbering is shown in Figure 1). Only electrode 3 is transmitting.

time-derivative of the pressure $\partial p/\partial t$ at these depths ($\lambda_3^* \approx 32\,\mu$m and $\lambda_1^* \approx 110\,\mu$m for depths up to 1.0 mm).

The number of active Rx-transducer elements i, the size of the FWHM of the respective responses I_i, and the relative strength between them influence the quality of the DAS generated images. Note that I_1 and I_5 are weak compared to the I_3 response from objects that are located at $L = 0.6$ mm, and are therefore less important when reconstructing such images. If the received echo signals are large compared to the noise level, a better image resolution can sometimes be achieved by weighting the responses I_i differently to adjust for the reduction of the signal strength related to the angles θ_i^L.

5. Discussion and Conclusion

Different ultrasound backscatter microscopes (UBM), operating at frequencies between 40 MHz and 100 MHz, were

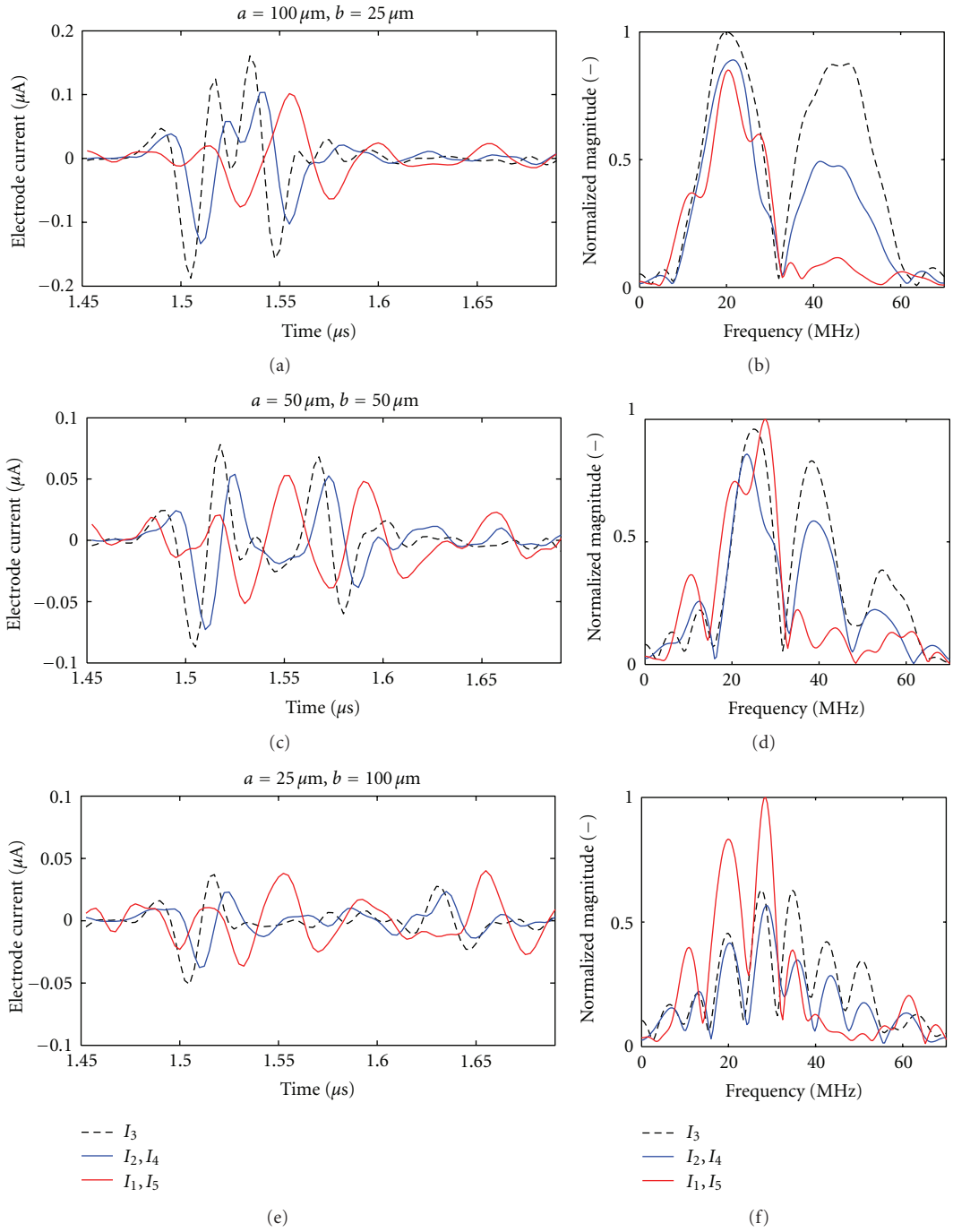

FIGURE 14: Electric currents generated at the five copper electrodes from acoustic echoes reflected by rectangular objects ($b \times a$) located at depth $L = 1.0$ mm (electrode numbering is shown in Figure 1). Only electrode 3, which is located directly in front of the object, is transmitting.

presented in [32]. A single, spherically shaped transducer system was used to generate focused beams while being moved mechanically along a linear path, transmitting every 4 μm. The measured spatial resolution of the B-scan images created from the system operating at 40 MHz was found to be 30 μm in the axial direction and 94 μm in the lateral direction. That is, similar to the resolution parameters ($\widehat{\lambda}_3$ and $\widehat{\lambda}_1$) obtained in this paper. Note that the axial and lateral resolution from a 92 MHz system was increased to 21 μm and 45 μm. However, these UBM systems have a fixed focal distance. The high image resolutions obtained with these systems are, therefore, limited to a narrower region (depth) than imaging systems based on phased transducer arrays with dynamic focusing properties. A prototype of a linear

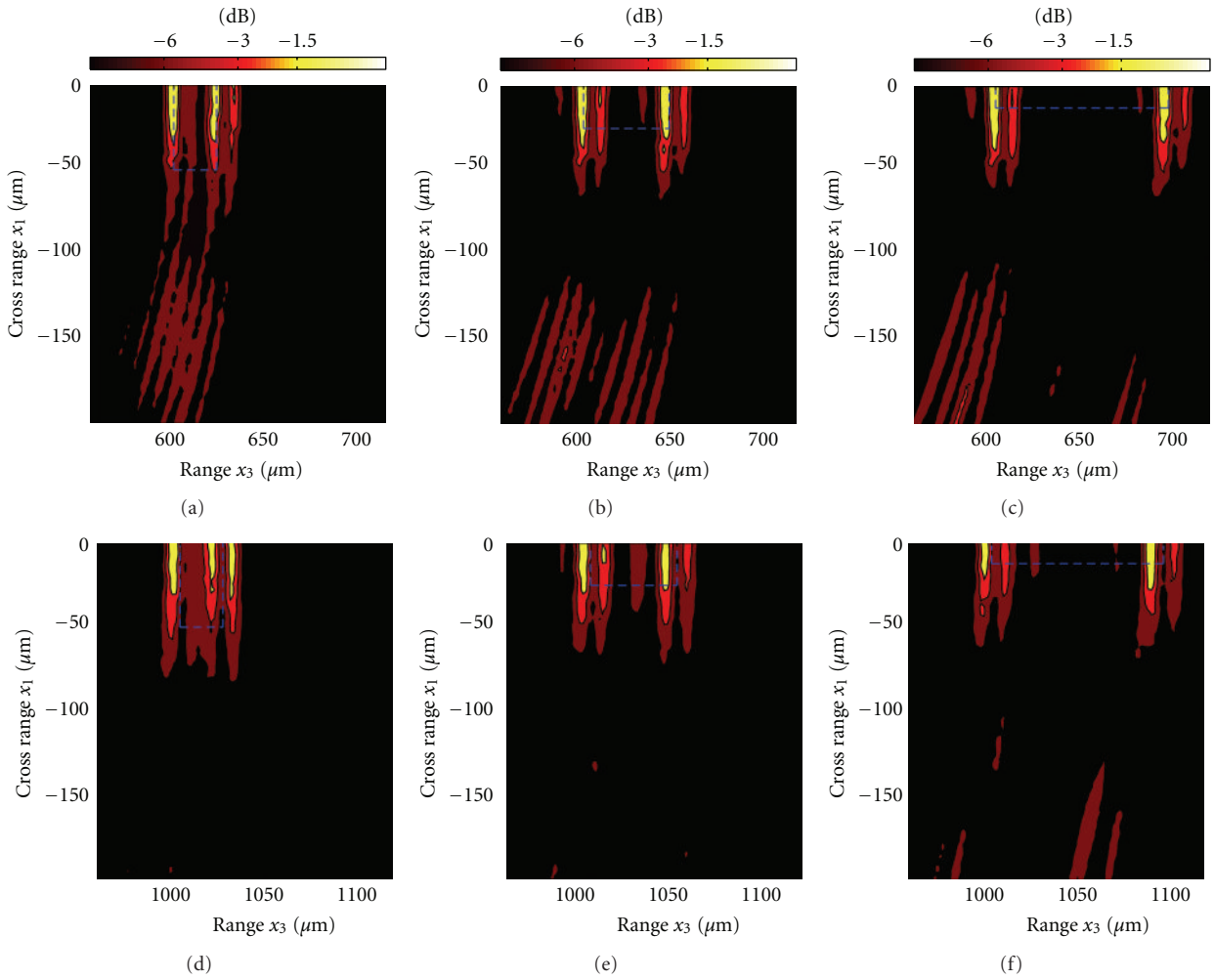

FIGURE 15: Images including the lower half of the objects (dashed blue lines) located at 0.6 mm depth (a, b and c) and 1.0 mm depth (d, e and f) and are reconstructed from a DAS scheme based on the currents plotted in Figures 13 and 14. The −1.5 dB, −3 dB (FWHM) and, −6 dB levels of the maximum are shown.

PVDF transducer array, electronically transmitting focused beams with center frequency around 25 MHz, produces images with a resolution of 100 μm axially and 400 μm laterally (at a depth of 15 mm) [33]. Another prototype, a linear transducer array based on a piezoelectric composite, operating around 30 MHz, was reported to produce images with both lateral and axial resolutions of approximately 100 μm, when using a synthetic aperture technique without Tx-beam steering [34]. The axial resolution $\widehat{\lambda}_3$ of the imaging system described in this paper, which operates with a center frequency of f_c, is close to V_{skin}/f_c. The images produced by these linear transducer array prototypes are far from having this high resolution relatively to the center frequency and must be further improved before they equal the high quality obtained by the UBM systems.

The image quality obtained from ultrasound scans, using the linear transducer system illustrated in Figure 1, has been evaluated by looking at numerical simulations based on FEM. Large attenuation in human skin and small responses from almost invisible objects (having small spatial dimensions and acoustic impedances similar to normal human skin) are factors which will reduce the signal-to-noise ratio and have to be overcome with highly sensitive electronics and sophisticated transducer designs. Objects with microscopic sizes can be vital in a medical diagnosis of human skin, and information like the size and geometry of different structures can be used in classifying and monitoring diseases. It is, therefore, important to have an ultrasound scanner that can produce high-resolution images (in both the axial and lateral directions).

Resolution parameters based on the pressure (FWHM of a Tx-focused beam) are often chosen as a measurement of a transducer system's image quality. Lateral resolution, axial resolution, and signal strength parameters of transducer systems with seven or less active (transmitting) transducer elements are plotted in Figures 10 and 11 for depths up to 3.0 mm and illustrate that the resolution of images obtained from an ultrasound scan depends both on the number of

active transducer elements and the skin depth. They also show that an array with five active transducer elements is sufficient for this system when scanning up to depths of 1.0 mm. Including more elements in the beam focusing does not affect the resolution quality significantly at such depths, since they only add relatively weak (low frequency) waves to the focused beam; for example, see Figure 7. The parameters given in Figure 11, which are based on the time-derivative of the pressure ($\partial p/\partial t$) beam profiles, were found to be in better agreement with the resolution obtained in reconstructed images based on synthetic Rx-beamforming. A large bandwidth is important, for example, the image resolution in the axial direction is mainly determined by the width of the pulse. The limiting resolution is in the lateral direction, which clearly suffers from the relatively large lateral dimensions of the individual transducer elements (electrodes that are 100 μm wide). However, at larger depths, the lateral dimension of the linear transducer array becomes the limiting factor. Better lateral beamforming in this region can be obtained by activating transducer elements further away from the focal point or by transmitting signals with different strengths. Other improvements can, for example, be achieved by reducing the electrode pitch and the width of the electrode lines (in the lateral direction).

Responses from ultrasonic scans of certain objects with rectangular cross sections are shown in Figures 13 and 14, using five active transducer elements. Images reconstructed from a synthetic DAS Rx-beamforming algorithm based on these responses are illustrated in Figure 15. Only the front and backside of these objects, which are parallel to the transducer array, appear in these images. The image quality is related to the localization errors of reconstructed (visible) structures. A different set of resolution parameters $\hat{\lambda}_3$ and $\hat{\lambda}_1$, related to the maximum spatial errors in both the axial and lateral directions of reconstructed images based on FWHM (-3 dB), is discussed. However, variations in the maximum localization errors of different skin structures illustrates that the quality of the images, according to this definition, depends on the objects under study. The localization errors of the structures studied in this paper (at depths around 0.5 mm and 1.0 mm) are $[\pm\hat{\lambda}_3/2, \pm\hat{\lambda}_1/2] \approx [\pm 15\,\mu\text{m}, \pm 40\,\mu\text{m}]$ or less in all the reconstructed images presented in Figure 15. Hence, $\hat{\lambda}_3$ and $\hat{\lambda}_1$ can be viewed as another set of resolution parameters and can also be interpreted as a measurement of the minimal distance between objects which can be resolved; that is, they will appear as two separated objects in the reconstructed images. The image quality will typically be increased by transmitting from more than one transducer element. Such Tx-Rx-beamforming has several advantages, including increased penetration depth and signal-to-noise ratio. For example, Tx-beamforming will increase the amplitude of the main lobe generated at the focal point as shown in Figure 11. The number of side lobes will be increased, but their gain in strength is typically severely less; see Figure 9. Images based on Tx-Rx-beamforming can be reconstructed synthetically from the responses created in systems, where all the involved elements in the Rx-beamforming are transmitting separately one by one. For example, by adding the DAS coordinate values obtained for each simulation with the synthetic Rx-beamforming algorithm described earlier.

The resolution parameters based on Tx-beamforming are perhaps the best description of a transducer array system's image quality, since they are computed without the influence from objects and, therefore, are unique for a transducer system. However, Figure 11 also illustrates how sensitive these FWHM definitions can be to small variations. The worst case Tx-beamforming resolution parameters based on time derivative of the pressure $\partial p/\partial t$ ($\lambda_3^* \approx 32\,\mu$m and $\lambda_1^* \approx 110\,\mu$m for depths up to 1.0 mm) were found to be similar to $\hat{\lambda}_3$ and $\hat{\lambda}_1$ derived from a resolution estimate of the images reconstructed with synthetic Rx-beamforming.

References

[1] F. S. Foster, C. J. Pavlin, G. R. Lockwood et al., "High frequency ultrasound backscatter imaging," in *Proceedings of the IEEE Ultrasonics Symposium*, vol. 2, pp. 1161–1169, Orlando, Fla, USA, December 1991.

[2] D. J. Weisbrod, C. J. Pavlin, K. Emara, M. A. Mandell, J. McWhae, and E. R. Simpson, "Small ciliary body tumors: ultrasound biomicroscopic assessment and follow-up of 42 patients," *American Journal of Ophthalmology*, vol. 141, no. 4, pp. 622–628, 2006.

[3] C. J. Pavlin and F. S. Foster, "Ultrasound biomicroscopy: high-frequency ultrasound imaging of the eye at microscopic resolution," *Radiologic Clinics of North America*, vol. 36, no. 6, pp. 1047–1058, 1998.

[4] A. Maxwell, S. W. Huang, T. Ling, J. S. Kim, S. Ashkenazi, and L. J. Guo, "Polymer microring resonators for high-frequency ultrasound detection and imaging," *IEEE Journal on Selected Topics in Quantum Electronics*, vol. 14, no. 1, pp. 191–197, 2008.

[5] M. Soldan, P. C. Silva, A. Schanaider, and J. C. Machado, "50 MHz ultrasound characterization of colitis on rats, in vitro," in *Proceedings of the IEEE Ultrasonics Symposium*, pp. 1967–1970, Beijing, China, November 2008.

[6] T. Yano, H. Fukukita, S. Ueno, and A. Fukumoto, "40 MHZ ultrasound diagnostic system for dermatologic examination," in *Proceedings of the Ultrasonics Symposium*, pp. 875–878, New York, NY, USA, 1987.

[7] D. M. Thiboutot, "Dermatological applications of high-frequency ultrasound," in *Medical Imaging: Ultrasonic Transducer Engineering*, Proceedings of SPIE, pp. 7–16, February 1999.

[8] N. Aspres, I. B. Egerton, A. C. Lim, and S. P. Shumack, "Imaging the skin," *Australasian Journal of Dermatology*, vol. 44, no. 1, pp. 19–27, 2003.

[9] J. Mamou, O. Aristizbal, R. H. Silverman, J. A. Ketterling, and D. H. Turnbull, "Highfrequency chirp ultrasound imaging with an annular array for ophthalmologic and small-animal imaging," *Ultrasound in Medicine and Biology*, vol. 35, no. 7, pp. 1198–1208, 2009.

[10] L. Zhang, X. Xu, C. Hu et al., "A highfrequency, high frame rate duplex ultrasound linear array imaging system for small animal imaging," *IEEE Ultrasonics Symposium*, vol. 57, no. 7, pp. 1548–1557, 2010.

[11] J. A. Brown, F. S. Foster, A. Needles, E. Cherin, and G. R. Lockwood, "Fabrication and performance of a 40-MHz linear array based on a 1–3 composite with geometric elevation

focusing," *IEEE Ultrasonics Symposium*, vol. 54, pp. 1894–1888, 2007.

[12] F. S. Foster, K. A. Harasiewicz, and M. D. Sherar, "A history of medical and biological imaging with polyvinylidene fluoride (PVDF) transducers," *IEEE Ultrasonics Symposium*, vol. 47, no. 6, pp. 1363–1371, 2000.

[13] J. A. Ketterling, O. Aristizábal, and D. H. Turnbull, "Polyimide backed 40-MHz PVDF transducers," in *Proceedings of the IEEE Ultrasonics Symposium*, vol. 1, pp. 117–120, 2005.

[14] K. E. Thomenius, "Evolution of ultrasound beamformers," in *Proceedings of the IEEE Ultrasonics Symposium*, vol. 2, pp. 1615–1622, 1996.

[15] N. N. Abboud, G. L. Wojcik, D. K. Vaughan, J. Mould, D. J. Powell, and L. Nikodym, "Finite element modeling for ultrasonic transducers," in *Medical Imaging 1998: Ultrasonic Transducer Engineering*, Proceedings of SPIE, pp. 19–42, usa, February 1998.

[16] D. Royer and E. Dieulesaint, *Elastic Waves in Solids II*, Springer, Paris, France, 1999.

[17] E. Brodal, J. S. Hesthaven, and F. Melandsø, "Numerical modeling of double-layered piezoelectric transducer systems using a high-order discontinuous Galerkin method," *Computers and Structures*, vol. 86, no. 17-18, pp. 1747–1756, 2008.

[18] M. D. Sherar and F. S. Foster, "The design and fabrication of high frequency poly(vinylidene fluoride) transducers," *Ultrasonic Imaging*, vol. 11, no. 2, pp. 75–94, 1989.

[19] D. Royer and E. Dieulesaint, *Elastic Waves in Solids I*, Springer, Paris, France, 1999.

[20] A. Yasmin and I. M. Daniel, "Mechanical and thermal properties of graphite platelet/epoxy composites," *Polymer*, vol. 45, no. 24, pp. 8211–8219, 2004.

[21] C. Nordling and J. Österman, *Physics Handbook for Sience and Engenering*, Studentlitteratur, Lund, Sweden, 1996.

[22] A. A. Volinsky, N. R. Moody, and W. W. Gerberich, "Interfacial toughness measurements for thin films on substrates," *Acta Materialia*, vol. 50, no. 3, pp. 441–466, 2002.

[23] C. Guittet, F. Ossant, L. Vaillant, and M. Berson, "In vivo high-frequency ultrasonic characterization of human dermis," *IEEE Transactions on Biomedical Engineering*, vol. 46, no. 6, pp. 740–746, 1999.

[24] Measurement Specialities, *Piezo Film Sensors Technical Manual, Internet Version*, Part 1 of 18, 1998.

[25] H. Y. Guney, "Elastic properties and mechanical relaxation behaviors of PVDF (poly (vinylidene fluoride)) at temperatures between −20 and 100°C and at 2 MHz ultrasonic frequency," *Journal of Polymer Science, Part B*, vol. 43, no. 20, pp. 2862–2873, 2005.

[26] J. Kulek, C. Pawlaczyk, and E. Markiewicz, "Influence of poling and ageing on high-frequency dielectric and piezoelectric response of PVDF-type polymer foils," *Journal of Electrostatics*, vol. 56, no. 2, pp. 135–141, 2002.

[27] P. E. Bloomfield, W. J. Lo, and P. A. Lewin, "Experimental study of the acoustical properties of polymers utilized to construct PVDF ultrasonic transducers and the acousto-electric properties of PVDF and P(VDF/TrFE) films," *IEEE Ultrasonics Symposium*, vol. 47, no. 1, pp. 1397–1405, 2000.

[28] T. D. Lhermitte, S. M. Handley, M. R. Holland, and J. G. Miller, "Anisotropy of the frequency-dependent ultrasonic attenuation inunidirectional graphite/epoxy composite material," *IEEE Ultrasonics Symposium*, vol. 2, pp. 819–823, 1991.

[29] P. Wu and T. Stepinski, "Quantitative estimation of ultrasonic attenuation in a solid in the immersion case with correction of diffraction effects," *Ultrasonics*, vol. 38, no. 1, pp. 481–485, 2000.

[30] J. L. Pons, H. Rodriguez, E. Rocona, J. F. Fernandez, and M. Villegas, "Practical consideration of shear strain correction factor and Rayleigh damping in models of piezoelectric transducers," *Sensors and Actuators A*, vol. 115, no. 2-3, pp. 202–208, 2004.

[31] E. Brodal, *Design characteristics related to performance of PVDF transducers used in non-destructive pulse-echo testing*, Ph.D. thesis, University of Tromsø, Tromsø, Norway, 2008.

[32] D. H. Turnbull, B. G. Starkoski, K. A. Harasiewicz et al., "A 40–100 MHz B-scan ultrasound backscatter microscope for skin imaging," *Ultrasound in Medicine and Biology*, vol. 21, no. 1, pp. 79–88, 1995.

[33] S. J. Carey, C. M. Gregory, M. P. Brewin, M. J. Birch, S. Ng, and J. V. Hatfield, "PVdF array characterisation for high frequency ultrasonic imaging," in *Proceedings of the IEEE Ultrasonics Symposium*, pp. 1930–1933, August 2004.

[34] T. A. Ritter, T. R. Shrout, R. Tutwiler, and K. K. Shung, "A 30-MHz piezo-composite ultrasound array for medical imaging applications," *Proceedings of the IEEE Ultrasonics Symposium*, vol. 49, no. 2, pp. 217–230, 2002.